Spectral Radiative Properties of Polydispersed SiO₂ Particle Beds

Chuyang Chen,[†] Chiyu Yang,[†] Devesh Ranjan,[‡] Peter G. Loutzenhiser,[‡] and Zhuomin M. Zhang[‡],^{*}

Georgia Institute of Technology, Atlanta, Georgia 30332-0405

The focus of this work is on the measurement and analysis of the radiative properties of polycrystalline SiO_2 particle beds with various layer thicknesses. The particles are polydispersed with average diameters of 222 μ m, 150 μ m, and 40 μ m. The spectral, directional-hemispherical reflectance and transmittance of the particle bed are measured at wavelengths from 0.4 μ m to 1.8 μ m using a monochromator, and the reflectance measurement is extended to 15 μ m using a Fourier-transform infrared spectrometer. Particles are closely packed between two transparent windows for measuring the radiative properties. In the visible and near-infrared region up to 1.8 μ m, the inverse adding-doubling method yields the effective absorption and scattering coefficients. The results suggest that short wavelength absorption needs to be included in modeling the behavior of particle beds due to multiple scattering. A discrete-scale Monte Carlo ray-tracing method is developed to model the radiative properties by assuming monodispersed spherical particles, and the simulated results compare well with measurements. The effective absorption and scattering coefficients of the particle beds obtained from the independent scattering theory are compared to those from the inverse method. The impact of dependent scattering on the packed beds is observed for smaller sized particles.

Keywords: absorption and scattering measurements, Monte Carlo method, packed bed, radiative properties, SiO₂ particles

[†] Graduate Research Assistant, George W. Woodruff School of Mechanical Engineering

[‡] Faculty Member, George W. Woodruff School of Mechanical Engineering

^{*}Corresponding Author. AIAA Associate Fellow. zhuomin.zhang@me.gatech.edu

Nomenclature

absorption coefficient, m⁻¹ a_{λ} $C_{\text{abs},\lambda} =$ absorption cross section, m² $C_{\text{sca},\lambda} =$ scattering cross section, m² effective particle diameter, m d = asymmetry factor g = Lparticle bed thickness, m = N particle number density, 1/m³ = complex refractive index = n real part of the refractive index =R directional-hemispherical reflectance = center of sphere location based on FCC \mathbf{r}_0 = center of sphere location after randomization $\mathbf{r}_{\rm c}$ =S specularity = location vector of a photon bundle S = directional-hemispherical transmittance T= direction vector of a photon bundle v = half of the clearance for particles between layers, m γ = δ step size of a photon bundle, m = ζ intercept distance, m = imaginary part of the refractive index K = λ wavelength, m = side length of a unit cell, m = reflectivity at the surface ρ = (isotropic or reduced) scattering coefficient, m⁻¹ σ_{λ} (true) scattering coefficient, m⁻¹ $\sigma_{\lambda,\text{true}} =$ optical thickness over a particle diameter $\tau_d = 4\pi\kappa d/\lambda$ τ_d particle volume fraction ϕ_{v} = uniformly distributed random number between 0 and 1 = χ scattering albedo Ø = Subscripts particle bed combined with the backside window bw = = windowed particle bed sample S window W = λ = spectral

I. Introduction

Radiative transfer in nonhomogeneous media including particle beds and porous structures plays an important role in the overall heat transfer processes for numerous aerospace and industrial applications (e.g., coatings [1], combustion or nuclear reaction furnaces [2,3], thermal barrier coatings [4], building and cryogenic insulation [2,5], and particle receiver and thermal energy storage in concentrated solar power [6–8]). For relatively small particles in a dilute suspension, the continuous-scale radiative transfer equation (RTE) is often applied to the participating medium (involving absorption, scattering, and emission) without considering inhomogeneity [9,10]. The absorption and scattering properties of individual particles (i.e., point scatters) are captured by the Mie theory, considering diffraction effect and then superimposed to obtain the properties of the medium according to the independent scattering theory [11–13]. When the particles are placed in close proximity, dependent scattering due to wave interference and near-field effects becomes important such that the simple superposition approach breaks down [14–16]. While RTE may be independently derived by performing an energy balance in a volume element along the ray propagation direction, it is essentially a far-field approximation of the rigorous electromagnetic wave theory [17,18].

Particle beds and porous media with particle/pore sizes from several tens to hundreds of micrometers are of great significance to contemporary technologies [13,19–25]. For relatively large particles or pores with dimensions much greater than the visible or infrared wavelengths, geometric optics is valid and the radiative properties can be modeled using the ray-tracing approach. The discrete-scale Monte Carlo method based on a stochastic sampling process is commonly applied to trace a large number of photon bundles (considering reflection/refraction at the interface and absorption inside an individual phase) to obtain the radiative properties of

particulate media [26–28]. More complicated models have been developed to include absorption by the hosting matrix (or semitransparent medium) [29–33]. The RTE is frequently applied to model the radiative properties by treating the particulate media as homogeneous with effective absorption and scattering properties. For spherical particles, the absorption and scattering cross sections as well as the scattering phase function of a single particle are commonly estimated by a Monte Carlo ray-tracing method. Then, the absorption and scattering coefficients of the particle beds are calculated using the independent scattering theory, similar to the situation with small particles [34,35]. However, even in the geometric-optics regime, multiple scattering or volume scattering due to the geometric proximity effect can also give rise to strong dependent scattering [28,36-39]. Some scaling factors have been suggested for the extinction coefficient or scattering albedo of particle beds with opaque spheres; however, no correlations or a clear trend exist for semitransparent spheres [36–38]. Hence, spatial or volume averaging techniques are often necessary to account for the dependent scattering effect for dense and complex structures [34,35,40–43]. Researchers have also used computer-assisted x-ray tomography to obtain 3D images of the microstructures in order to retrieve the effective absorption and scattering properties of an element volume [21,41].

Most studies are based on numerical simulations and comparisons between different models [21,28–32,40–43]. Experimental investigations have been limited, especially for particle sizes much greater than the wavelengths of interest. Brewster and Tien [14] and Yamada et al. [15] measured light scattering at two visible wavelengths for polymer particle bed with particle diameters of 80 nm, 2 μm, and 11 μm with varying volume fractions. Agarwal and Mengüç [12] gave a summary of earlier experimental researches on light propagation in participating media and performed an extensive theoretical and experimental study of the angle-resolved scattering by

mono- and poly-dispersions of suspended particles. Kamiuto et al. [37,44] measured the extinction coefficient, albedo, and phase function of packed spherical particle beds with both opaque and transparent particles of diameters near 1 mm. Their results provide experimental evidence of dependent scattering due to volume scattering effect for large spheres in the geometric optics regime. A number of studies are based on the inverse solutions to retrieve the absorption and scattering coefficients and/or phase function from experimental data for porous ceramic [4,45–48], open-cell foam insulation [49,50], aerogel [5], bubbles in fused quartz glass [20], sintered porous plastics [51,52], and turbid media or biological skins and tissues [53,54]. The inverse methods include the simple two-flux model, three-flux model, the discrete-ordinates method (DOM), the adding-doubling (AD) method, among others [9,10,13,53]. The experimental data that are most frequently used are the spectral, directional-hemispherical reflectance and transmittance of the specified media in a flat plate or disk geometry [48,52]. Researchers have also used collimated transmittance and/or angle-resolved scattering properties [12,14,51,55–57].

Radiative properties of particle beds with configurations that facilitate practical applications with polydispersed, mixture types, and irregular shapes have also been investigated [58–61]. Lipiński et al. [58] and Jäger et al. [59] measured the transmittance of polydispersed packed beds with a mixture of SiO₂, ZnO, and C particles of different sizes and volume fractions at a wavelength of 632.8 nm. As more ZnO and C contents are added into the SiO₂ bed, the measured transmittance reduces rapidly, and the absorption is expected to increase. To determine the scattering phase function, Coray et al [60] and Marti et al. [61] performed spectral angle-resolved measurements of packed beds of ZnO particles and SiC particles, respectively. The effect of hosting medium was examined by embedding the SiC particles in an epoxy resin [61].

Further investigation of the radiative properties of polydispersed particle beds is necessary, especially in the semitransparent region and at mid-infrared wavelengths. Outstanding questions remain as to whether simplified models are adequate to explain the measured spectral, directional—hemispherical transmittance and reflectance, whether isotropic scattering model can be used in the continuous-scale modeling, and whether it is appropriate to use spherical particles with an average diameter to represent the packed bed with irregularly shaped particles for prediction of the hemispherical radiative properties. The impact of dependent scattering on the radiative properties for semitransparent particles and the influence of impurity on the absorption need to be further analyzed based on experimental findings.

In this work, the room-temperature spectral radiative properties of packed beds made of polydispersed, irregular particles in the wavelength (λ) region from 0.4 µm to 15 µm are measured using a windowed method with two spectrometers. Polycrystalline SiO₂ particles are selected because they are mechanically and chemically stable, transparent to visible to near-infrared light, commercially available in various sizes. SiO₂ particles are also used to form many technologically important particles such as ceramic and mullite particles [7–9,24,25]. Three types of particles with average diameters (d) of 222 µm, 150 µm, and 40 µm are used to form densely packed (volume fractions from 60-72%) particle beds whose thicknesses (L) vary from approximately 1 mm to 6 mm. In the shorter wavelength region from 0.4 µm to 1.8 µm, the particle bed is semitransparent. The absorption and scattering coefficients of each type of particles are extracted from the measured transmittance and reflectance using an inverse method. For opaque particle beds (L = 6.2 mm), the reflectance is measured up to λ = 15 µm. The radiative properties of the particle beds are modeled with a discrete-scale Monte Carlo method assuming monodispersed spheres with a specularity parameter (S) to partially account for the shape and size irregularity. The simulated results are

compared with the measurements to examine the applicability and limitations of the Monte Carlo modeling. To understand the dependent scattering effect, the absorption and scattering coefficients are also obtained from the independent scattering theory based on the particle volume fraction, average diameter, and the scattering and absorption cross sections predicted by the Monte Carlo model for a single sphere.

II. Methodology

The particle characterization and sampling method used in the spectroscopic measurements are described in Secs. II.A and II.B, respectively. An inverse solution technique that combines the (forward) adding-doubling and inverse adding-doubling (IAD) methods is employed to obtain the absorption and scattering coefficients in accordance with the continuous-scale RTE from the measured transmittance and reflectance, as outlined in Sec. II.C. The discrete-scale Monte Carlo simulation provides a direct and more intuitive simulation of the radiative properties of the particle bed, and the algorithm used in the present study is elaborated in Sec. II.D.

A. Particle Characterization

Polycrystalline SiO₂ particles of different sizes are used to form the packed bed samples with different thicknesses. Three types of particles are chosen based on the average diameters: (1) Type A ($d = 222 \mu m$), (2) Type B ($d = 150 \mu m$), and (3) Type C ($d = 40 \mu m$). Type A particles are round grain silica sand manufactured by Wedron Silica Co. (Wedron 410), with ~ 99.65% purity. The Wedron 410 particles are jet milled to produce power with an average diameter of ~ 40 μm , which are identified as Type C in this study. Type B particles are obtained from US Research Nanomaterials, Inc. They were manufactured the airflow crushing method from large quartz

particles with a purity > 99.5%. The microscopic images of these particles are shown in Fig. 1. It can be seen that Type A particles are more uniform and spherical, Type B particles exhibit more irregularities and contain additional impurities, and Type C particles are powder-like with irregular fragments and flakes. The diameters for Type A or B particles are determined by volume averaging using the sieve filtration method. A nominal diameter based on microscopic images is used for Type C particles. A small fraction of other oxides (*i.e.*, Al₂O₃, TiO₂, and Fe₂O₃) is present, resulting in weak absorption in the visible and near-infrared regions.

B. Windowed Method

The particles are encased in a windowed sample holder, consisting of two transparent layers (front and back) and a spacer ring of various thicknesses, as shown in Fig. 2a with fused quartz windows for measurements from 0.38 μ m to 1.8 μ m using a monochromator. For midinfrared measurements using a Fourier-transform infrared spectrometer (FTIR), ZnSe windows are used to hold the particles. The directional-hemispherical transmittance or reflectance is measured by placing the sample at the front or back of an integrating sphere, as shown in Fig. 2b, with suitable references. The windowed method was calibrated and used by the authors to measure bauxite particles [25]. To measure the reflectance, the sample holder is tilted by \sim 7° so that the specular component is also included. Once the sample holder is filled with particles, the particle bed has the same thickness as the spacer ring with nominal thicknesses: L = 1.0 mm, 1.6 mm, 3.4 mm, and 6.2 mm. The actual spacer thicknesses are 0.97±0.01 mm, 1.61±0.02 mm, 3.37±0.03 mm, and 6.23±0.03 mm as measured with a caliper. Only nominal thicknesses are referred to hereafter for clarity. The particle volume fractions (ϕ_v) are measured and averaged over all thicknesses for each type of particles and the results are tabulated in Table 1. Due to irregular shapes,

polydispersed condition and different sample fabrication processes, no apparent relation between ϕ_v and d is observed. Nevertheless, the particles are densely packed and a validation by Monte Carlo ray-tracing method showed a very small impact for the range of ϕ_v studied in this work. Reflectance and transmittance measurements are performed on multiple spots of the sample and the averaged results are used to mitigate the impact of localized packing unevenness.

The net radiation method is used to determine the (directional-hemispherical) reflectance and transmittance of the particle bed. Since the packed bed is considered as semitransparent, the recursive formulation is used to obtain the properties of the particle bed from the measured properties of the "sample" that include the particle bed sandwiched between two windows. For a packed bed layer on a window only, the reflectance and transmittance of the "bed/window" may be expressed, respectively, as [10]

$$R_{\rm bw} = R + \frac{R_{\rm w}T^2}{1 - R_{\rm w}R}$$
 and $T_{\rm bw} = \frac{T_{\rm w}T}{1 - R_{\rm w}R}$ (1)

where *T* and *R* without subscripts are for the packed bed, subscript w signifies window, and subscript bw stands for the bed/window composite. The measured sample reflectance and transmittance as functions of the properties of the window, packed bed, and bed/window are given, respectively, by [10]

$$R_{\rm s} = R_{\rm w} + \frac{R_{\rm bw} T_{\rm w}^2}{1 - R_{\rm w} R_{\rm bw}} \quad \text{and} \quad T_{\rm s} = \frac{T_{\rm w} T_{\rm bw}}{1 - R_{\rm w} R_{\rm bw}}$$
 (2)

With the predetermined $R_{\rm w}$ and $T_{\rm w}$ of the window material, Eq. (2) is solved for $R_{\rm bw}$ and $T_{\rm bw}$ using the measured $R_{\rm s}$ and $T_{\rm s}$. The calculated results are then plugged into Eq. (1) to obtain the radiative properties of the particle bed, R and T. Note that all R's and T's are

directional-hemispherical properties at a specified wavelength with the subscript λ being omitted for simplicity.

When the transmittance of the particle bed is negligibly small, the above equations reduce to the following for an opaque packed bed:

$$R_{\rm s} = R_{\rm w} + \frac{T_{\rm w}^2 R}{1 - R_{\rm w} R} \tag{3}$$

Measurements are performed on two spectrometric instruments that in combination cover the spectral range 0.4 $\mu m \le \lambda \le 15$ μm . A grating monochromator uses a 200-mm-diameter integrating sphere whose inner surface is made of polytetrafluoroethylene (PTFE), and a Si and Ge photodetector for the visible and near-infrared measurements up to $\lambda = 1.8$ μm . A 10-mm-thick sintered PTFE plate is used as the reflectance reference. A liquid-nitrogen-cooled MCT detector is used together with the FTIR and a 150-mm-diameter gold-coated integrating sphere to measure the directional–hemispherical reflectance for 1.6 $\mu m \le \lambda \le 15$ μm . A gold-plated reference is used with 95% diffuse reflectance. Data averaging is used in the measurement to analyze the results from both instruments in order to increase the signal-to-noise ratio. The uncertainties associated with the measurements at 95% confidence level are \pm 0.01 in transmittance and \pm 0.02 in reflectance for the monochromator measurements, and \pm 0.03 in reflectance for the FTIR measurements. A detailed description of the two instruments may be found from Refs. [25,52].

C. Forward and Inverse Adding-Doubling Methods

For a cold medium (without emission) with layered geometry (each layer is homogenous), the AD method allows the directional-hemispherical radiative properties to be evaluated with similar accuracy as the DOM in solving RTE using much less computational time and memory

[53,54]. In the doubling method, the reflection and transmission of a slab twice as thick is found by placing two identical thin slabs and adding the contributions from each slab where the reflectance and transmittance are obtained by integrating over all angles. The adding algorithm extends the method to dissimilar materials used in each layer. The AD method takes into consideration of surface reflection/refraction and anisotropic scattering, providing a more accurate solution than the two-flux model. The input parameters for a single slab or particle bed are the (effective) absorption coefficient (a_{λ}), scattering coefficient (σ_{λ}), refractive index, and the scattering phase function. For anisotropic scattering, the simple Henyey–Greenstein (HG) phase function is often used to distinguish the contributions of the forward and backward scattering with an asymmetric factor (g) [9,56]. In the present study, the effective refractive index of the bed is assumed to be unity and boundary reflections are neglected.

Alternatively, if R and T and thickness are known, the inverse method can be used to retrieve a_{λ} and σ_{λ} [48,52–54]. A set of a_{λ} , σ_{λ} , and g based on the initial guess is used to perform the AD calculation (g=0 corresponds to isotropic scattering). The R and T calculated from AD are compared with the measurements to update the parameters iteratively until the difference between the AD prediction and the measurement is smaller than a preset tolerance. In the absence of angular resolved measurement (e.g., the collimated or normal-to-normal transmittance of the slab], no unique set of parameters a_{λ} , σ_{λ} , and g can be determined as only two input parameters R and T for a given thickness are available. Details of the AD and IAD algorithm and software can be found online [62]. For highly scattering media, a scaling effect is present such that R and T depend only on the absorption coefficient and reduced scattering coefficient. The reduced scattering coefficient is defined as $\sigma_{\lambda} = \sigma_{\lambda, \text{true}}(1-g)$, which may be

viewed as equivalent scattering coefficient for isotropic scattering. Here, $\sigma_{\lambda, \rm true}$ is the "true" scattering coefficient to go with the HG phase function. By setting g=0 in the IAD, the equivalent scattering coefficient σ_{λ} is then obtained (which is the same as $\sigma_{\lambda, \rm true}$ for isotropic scattering case). The IAD calculation potentially yields multiple solutions due to measurement uncertainty for very small T (< 5%). Hence, care must be taken to determine the physically correct set of solutions (i.e., a_{λ} and σ_{λ}).

D. The Monte Carlo Method

The discrete-scale Monte Carlo simulation is based on tracing the rays (or photon bundles) through the inhomogeneous medium considering reflections and refractions at the boundary and absorption inside the particle. A randomly packed SiO₂ particle bed is generated assuming that all the SiO₂ particles are spherical with equal diameter. The generation of the spheres starts with the basic arrangement scheme of a face-centered cubic (FCC) cell [63] with a default vector $\mathbf{r}_0 = \langle x_0, y_0, z_0 \rangle$ at each sphere center. The particle volume fraction is given by

$$\phi_{v} = \frac{2\pi}{3} \left(\frac{d}{\xi}\right)^{3} \tag{4}$$

where ξ is the length of a unit cell that contains four spheres. The adjacent particles (or spheres) in a standard FCC arrangement touch each other, resulting in $\phi_v = 74\%$. The particles no longer touch and the volume fraction decreases when ξ is extended. Other basic schemes may also be used such as the simple cubic and body-centered cubic [28]. However, the FCC arrangement produces the highest ϕ_v without overlapping spheres.

Since the x-y dimension is much larger than the beam spot, it is assumed to be infinitely extended. In the modeling, period boundary conditions are applied to ensure that each photon bundle only terminates by absorption or exiting from the top layer (reflected) and bottom layer (transmitted). A unit column ($\xi \times \xi \times d$) is constructed layer-by-layer along the z-direction until the thickness reaches the prescribed bed thickness. If the photon bundle hits the side of the unit column before exiting, it is reintroduced to unit column via the periodic boundary condition until it is either absorbed or escapes. The center of each sphere is randomly shifted in the x-y plane within the margins for a bed that is not closely packed. The new central location $\mathbf{r}_c = \langle x_c, y_c, z_c \rangle$ is calculated by

$$\begin{cases} x_{c} = x_{0} + \gamma (2\chi - 1) \\ y_{c} = y_{0} + \gamma (2\chi - 1) \\ z_{c} = z_{0} \end{cases}$$
 (5)

where χ denotes a random number from 0 to 1, and γ is half of the clearance between particles in adjacent layers from an FCC arrangement to ensure no overlapping of particles. The randomization is applied simultaneously for all particles on one layer with different random numbers for each direction, and a new set of random numbers is regenerated for each subsequent layer to ensure no overlapping particles along with a certain degree of randomness. Without randomization, even beds of high particle volume fraction permit direct light transmission in regular FCC arrangement. To further ensure the randomness of the bed, after a certain number of photon bundles been traced, say 10, the random bed is regenerated according to Eq. (5).

In this work, the photon bundles are launched above the unit column (analogy to particle bed when viewed as periodic structure) with 7° incidence along z-axis at a random location on the x-y plane confined by the cell side length ξ . This angle is chosen to be consistent with the

reflectance measurement by the integrating sphere. The results for incidence angles from 0° to 10° are essentially the same (within the statistical uncertainty). The gas medium (air) is assumed nonparticipating. Photon bundles travel within the bed and are subject to interception by particles or side boundaries of the unit column. The path of a photon bundle is described by the starting point with coordinates $\mathbf{s} = \langle s_x, s_y, s_z \rangle$ and a direction unit vector $\mathbf{v} = \langle v_x, v_y, v_z \rangle$. Interception by a side boundary, (x, y) = (0, 0), $(0, \xi)$, $(\xi, 0)$, or (ξ, ξ) , triggers periodic boundary condition. Interceptions by particles (spherical surface) are modeled by reflection or refraction at the interface. The determination whether the photon bundle is reflected or refracted is realized by calculating the surface reflectivity, ρ , averaged from two polarizations based on the Fresnel equations using) [63]. A newly generated χ is compared the complex refractive index of the particle (\tilde{i} with ρ such that reflection occurs when $\chi < \rho$ and otherwise refraction occurs. For refracted photon bundles that enter the particle, a similar process is followed with the next interception on the spherical surface. Due to the crystalline nature of SiO₂, the photon bundle travels in a straight line inside of the particle. The attenuation is governed by the absorption index (κ) and the step size of a photon bundle is calculated from

$$\delta = \frac{\lambda}{4\pi\kappa} \ln(\chi) \tag{6}$$

where δ denotes a step size that a photon bundle may travel during each sub-level iteration within the sphere, and χ is a newly generated random number. When absorption is negligible (i.e., $\kappa \approx 0$ and $\delta \to \infty$), the photon bundle may experience multiple reflections within the sphere but will eventually escape the sphere.

When tracing photon bundles outside of a particle (while still in the particle bed), the interception distance to a specific particle is calculated as:

$$(s_{x,\text{new}} - r_{x,c})^2 + (s_{y,\text{new}} - r_{y,c})^2 + (s_{z,\text{new}} - r_{z,c})^2 = (d/2)^2$$
 (7)

$$s_{x,\text{new}} = s_x + v_x \zeta$$
, $s_{v,\text{new}} = s_v + v_v \zeta$, and $s_{z,\text{new}} = s_z + v_z \zeta$ (8)

where ζ is an intercept distance, and $\langle s_{x,\text{new}}, s_{y,\text{new}}, s_{z,\text{new}} \rangle$ denotes the new location vector. These relations reduce to a quadratic equation with two solutions (including the complex numbers and negative numbers) of ζ for each sphere in the unit column. Since ζ must be a real positive number, the smallest value corresponds to the closest particle that intercepts the photon bundle along the direction of propagation. The photon bundle may be intercepted by the side of the unit column before reaching a sphere; in such case, the periodic boundary condition is applied to redirect the photon bundle to the unit column. This is to say that $0 \le s_x$ (or $s_{x,\text{new}}$) $\le \xi$ and $0 \le s_y$ (or $s_{y,\text{new}}$) $\le \xi$, regardless of their actual location in the global coordinates.

Tracing rays in a highly absorbing sphere (e.g., near a phonon mode) becomes difficult as the refracted wavevector has significant imaginary component and the refraction angle becomes complex. Therefore, an optical thickness based on the diameter is defined as $\tau_d = 4\pi\kappa d/\lambda$ to determine whether the particle medium is regarded as opaque or semitransparent since the internal transmissivity is $\exp(-\tau_d)$ for a path length of d. For $\tau_d >> 1$, the particle is considered as opaque and refraction is treated as absorption without further tracing. The surface reflectivity is calculated using the complex refractive index. For $\tau_d < 1$, in general, $\kappa << n$; hence, only n is used when calculating the surface reflectivity and the refraction angle. The real refraction angle enables further ray tracing inside the particle following Eq. (6) to account for internal absorption.

Due to irregular shapes of particles and polydispersed nature of the particle bed, a specularity parameter $S \in [0,1]$ is introduced to partially account these effects by allowing the

photon bundles to specularly or diffusely reflect. A random number is compared with S to determine specular ($\chi < S$) or diffuse ($\chi > S$) reflection and refraction when launching a photon bundle. The surface condition is then regarded as perfectly specular or diffuse until the next photon bundle is generated. The total number of photon bundles used in the calculation is typically 10^5 . It takes 10 runs to obtain the average and standard deviation in order to check the statistical variation and ensure reasonable outcome. In the semitransparent region, it takes a much longer time to perform the ray tracing for each photon bundle. Therefore, the total number of photon bundles is reduced to improve the calculation speed without significantly reducing the computational accuracy.

III. Measurement Results, Analysis, and Comparison with Modeling

The measured reflectance spectra for particle beds of different types are compared with a plate sample to illustrate the scattering and size effects on the radiative properties as discussed in Sec. III.A. The absorption and scattering coefficients obtained from the IAD method and the comparison of the calculated radiative properties with measurements are presented in Sec. III.B. The Monte Carlo simulation results are compared with experiments in Sec. III.C.

A. Measured Reflectance Spectra

The reflectance in the spectral region 0.4 μ m < λ < 15 μ m of the particle bed with L=6.2 mm is shown in Fig. 3 for all three types of particles, identified by the average particle diameter. At such thickness, the particle beds are essentially opaque. Note that R is deduced from the measured windowed sample reflectance considering properties of the fused quartz or ZnSe windows in different spectral region [25]. Due to the difference in measurement uncertainty and

decreased signal-to-noise ratio near the spectral limits of the instruments, the results for 0.4 μ m < λ < 1.8 μ m are based on monochromator measurements, and results for 1.9 μ m < λ < 1.5 μ m are based on the FTIR measurements. A linear interpolation is used for 1.8 μ m < λ < 1.9 μ m to smoothly merge the two spectra. For comparison purpose, the calculated R for a 6.2-mm-thick flat SiO₂ plate is shown in Fig. 3, considering the ordinary and extraordinary effective dielectric functions of α -quartz [25,63]. The optical constants are mainly taken from Philipp [64] with some modifications on κ from 2.7 μ m to 5.0 μ m, considering impurity absorption [65–67].

In the region for 0.4 μ m < λ < 5 μ m, the plate sample is transparent or semitransparent with a low R (< 10%) because of the small refractive index of the polycrystalline silica (n < 1.6). When n decreases to unity at $\lambda \approx 7.3$ μ m, R = 0 (*i.e.*, the Christiansen effect) [63]. Particle scattering causes significant enhancement in R at short wavelengths, especially with Type C particles (d = 40 μ m). This is a well-known phenomenon: a high reflectance (\approx 99%) has been demonstrated using micron-sized glass spheres for daytime radiative cooling purpose [68]. Due to impurity absorption, R for the particle beds drops quickly toward shorter wavelengths when λ < 1 μ m. This is not observed for pure α -quartz plate samples. There is a dip for 2.7 μ m < λ < 3.4 μ m in R due to OH stretching [67]. Scattering causes high R for 3 μ m < λ < 5 μ m and even near the Christiansen wavelength for Type C particles.

Near the phonon reststrahlen absorption band (8 μ m < λ < 10 μ m), κ > n and surface reflectivity becomes very high. All particles and plate samples are considered as opaque in this region since the photon penetration depth, $\lambda/(4\pi\kappa)$, is less than 1 μ m. The opaque particles form cavity structures that traps the incoming photons, enhancing absorption [63]. Smaller particles with more irregularities effectively trap more photons. In addition, wave effects also potentially play a role at longer wavelengths. This provides a qualitative explanation of the reduction of reflectance

with the particle bed, especially for smaller sized particles. The features at $\lambda > 10$ µm are more complicated and not easily explainable. For the plate sample, additional phonon resonances exist and the effects appear to be evened out with the particle beds. Wave effects cannot be neglected, and the reflectance does not vary monotonically as a function of the particle size.

B. Absorption and Scattering Coefficients Obtained from IAD

Both R and T are measured from 0.4 μ m to 1.8 μ m to further characterize the particle beds of different thicknesses. The effective absorption and scattering coefficients (*i.e.*, a_{λ} and σ_{λ}) are retrieved from the measured R and T for a given thickness using IAD as described previously. For Type A particles, the obtained a_{λ} and σ_{λ} are averaged at each wavelength for L=1.0 mm, 1.6 mm, and 3.4 mm, and then fitted to a polynomial function to obtain smooth functions. Due to the low transmittance at shorter wavelengths, the results for L=6.2 mm is excluded. For Type B particles, T is measured only for L=1.0 mm since it is very low for other thicknesses and completely opaque when L=6.2 mm. For Type C particle, T is negligibly small when $L \ge 1.6$ mm. Therefore, the IAD is only applied to the packed beds with L=1.0 mm for Type B and C particles to obtain a_{λ} and σ_{λ} . The polynomial coefficients obtained from fitting are listed in Table 1 for all samples.

The measured R and T for Type A particles are shown (dashed lines) in Fig. 4, and the results calculated with AD using the fitted a_{λ} and σ_{λ} are also shown (solid lines). The measurements exhibit some discontinuities about $\lambda=1$ μ m due to the switching between the Si and Ge photodetectors and associated filter and grating sets. A dip is observed near $\lambda=1.4$ μ m in both T and R, presumably due to defect absorption of these particles. Deviations between the

measured and calculated results are mainly attributed to sample-to-sample variations, experimental uncertainties, and regression errors. The root-mean-square deviation (RMSD) between the measurement and calculation is 0.031 in T with L=1.6 mm, and 0.016 if the R and T for all thicknesses are considered. In general, both R and T decrease towards shorter wavelengths, indicating a strong impurity absorption feature especially for $\lambda < 1$ μ m. The R value for L=6.2 mm is very close to that for L=3.4 mm and is, therefore, not shown in Fig. 4a. As shown in Fig. 4b, T for the L=6.2 mm bed is negligibly small in the visible region and less than 8% for λ up to 1.8 μ m. For L=1 mm at $\lambda=0.4$ μ m, $R\sim0.41$ and $T\sim0.23$, resulting in an absorptance (1 -T-R) of 0.36. In the visible region, increasing L gives rise to an increase in R with a faster decrease in T. The net result is an increase in the absorptance as L increases until the packed bed becomes opaque.

Similar results for Type B and C particles are shown in Fig. 5. For Type B, R slightly increases from L=1 mm to L=6.2 mm, as shown in Fig. 5a. For Type C particles, R is only shown for L=1.0 mm because it is essentially the same for L=6.2 mm. For smaller sized particles, T is very low even with L=1 mm, as shown in Fig. 5b. Both R and T increase quickly from $\lambda=0.4$ µm to 0.8 µm. Note that R for Type C is much higher than that for Type A and B due to the stronger scattering effect with smaller particles. The RMSD is ≤ 0.01 with Type B and C particles.

The absorption and scattering coefficients calculated using the polynomial coefficients listed in Table 1 are plotted in Figs. 6a and 6b, respectively. For all three type of particles, a_{λ} increases rapidly towards shorter wavelengths. The relatively large values for Type B particles ($d=150~\mu m$) indicates that Type B particles possess more impurity than Type A and C particles. The absorption coefficient for Type C particles is almost the same as for Type A particles for 1.2 μm < λ < 1.8 μm but much larger towards the shorter wavelengths. At λ = 0.4 μm , a_{λ} = 0.28 μm

and 0.8 mm^{-1} for Type A and C particles, respectively, even though the intrinsic properties of the particles for Type A and C are the same. As seen from Fig. 6b, σ_{λ} is almost independent of the wavelength for Type A and B; however, it increases towards shorter wavelengths for Type C and is much larger than those of Type A and B. The IAD solutions inherently account for any dependent scattering effects or wave effects, though it does not treat them separately. The effect of dependent scattering will be addressed in Sec. IV.

The magnitude of σ_{λ} is 2 to 3 orders of magnitude higher than a_{λ} . The scattering albedo $\omega = \sigma_{\lambda}/(a_{\lambda} + \sigma_{\lambda})$ is shown in Fig. 6c with a scale minimum of 0.88. It can be seen that ω increases towards longer wavelengths and reaches 0.98 with Type A and B particles. With Type C particles, $\omega \approx 0.99$ at $\lambda = 0.4$ µm and increases to 0.999 at $\lambda = 1.8$ µm. The implication of the effective absorption and scattering properties is that a forward calculation may be employed to model radiative transfer in packed beds of similar particle type and volume fractions for the calculation of solar absorptance and effective conductivity of densely packed beds [6–8].

C. Monte Carlo Simulation and Comparison with Measurements

The input parameters for the Monte Carlo simulation of spherical particles are d, ϕ_v , L, S, and the complex refractive index of SiO₂. Pure SiO₂ with a bandgap near 9.5 eV is highly transparent from the ultraviolet to the near-infrared (150 nm to 2.5 μ m) [64,65]. The effective absorption index κ of the SiO₂ particles is estimated in the short wavelength region to account for impurities. A trial-and-error process is performed on the L=1 mm case of Type A and B to obtain κ at a prescribed wavelength. Type C particles are assumed to possess the same optical constants as Type A. In the visible region from 0.4 μ m to 0.7 μ m, the average κ is 5 × 10⁻⁶ for Type A and

 9×10^{-6} for Type B. Higher κ values for Type B particles are consistent with the higher absorption coefficient of the packed bed observed in Fig. 6. The photon penetration depth inside SiO₂ varies from about 4-40 mm for 0.4 μ m < λ < 1.4 μ m. The absorption is greatly enhanced due to scattering, causing a reduction of the transmittance of the packed bed with small particles.

The specularity parameter S is also treated as a fitting parameter that is independent of the wavelength but dependent on the particle type and thickness of the bed thickness. For Type A, S = 0.45 is used for L = 1.0 and 1.6 mm, and S = 0.25 is used for L = 3.4 and 6.2 mm to obtain good agreement between the simulated and measured T and R for 0.4 µm $< \lambda < 1.8$ µm. Jeong et al. [56] measured the scattering phase function of a single layer of Wedron 410 particles (*i.e.*, Type A), and obtained S = 0.8 by fitting the phase function with a Monte Carlo modeling. The dependence of S on the layer thickness manifests a geometric multiple scattering effect in the packed bed. The decreased S suggests that particles scatter more diffusely for thicker beds when scattering tends to become more isotropic. The assumption of spherical particles in a FCC arrangement does not fully represent the actual topography and arrangement of particles. Hence, S is taken as an adjustable parameter that enables better agreement between the simulation and the experiments. For Type B and C particles, S = 0 (completely diffuse) is obtained due to their large irregularities.

The comparison results are shown in Fig. 7 for all samples with the Monte Carlo simulation (model) shown as solid lines and experiments as dashed lines. Since R for L=6.2 mm with Type A is very close to that for L=3.4 mm, it is not shown. Some fluctuations is observed in the model due to statistical noise. The RMSD between the model and experiment is typically ~ 0.02 , which is comparable with the experimental and numerical uncertainties. However, the model overpredicts T when the measured transmittance is relatively low. The reason is attributed to the blockage and additional scattering by polydispersed particles with shape irregularities in the actual packed bed

that is not fully captured by the Monte Carlo model. Despite the simplifications, the discrete-scale Monte Carlo model allows quantitative prediction of the radiative properties in the visible and near-infrared region.

The Monte Carlo method is also used to model R up to $\lambda \approx 15 \mu m$ using the previously obtained S. Only the cases of L = 6.2 mm are measured with FTIR at longer wavelengths. The measurement and model are compared in Fig. 8. As previously seen from Fig. 3, due to the competing effect of absorption and scattering by particles of different sizes, R is similar for Type A and B when $\lambda < 1.8 \,\mu m$. Whereas smaller particles tend to scatter more and produce higher reflectance, the absorption in Type B particles are stronger due presumably to the additional impurities. For 2.7 μ m < λ < 5 μ m, the absorption bands of α -quartz are rather complicated [66,67]. For this reason, the value of κ is slightly adjusted for Type A to achieve a better agreement in R between the model and measurement. These values are used for Type B and C due to insufficient information or reasoning necessary to fine tune the parameters for matching. The trend correlates well between the model and measurement as shown in Figs. 8b and 8c. Another notable feature is that, in the phonon resonance band between 8 µm and 10 µm, the model produces a much higher R that is almost independent of the particle size. Based on the geometric optics, because the SiO₂ particle is opaque in this region (the photon penetration depth is less than 2 µm), scattering occurs by surface reflection in the top few layers until the beam is completely blocked. Multiple reflections occur on rough or curved surfaces that enhance absorption via the cavity effect [9,10,63]. The monodispersed spheres used in the Monte Carlo model do not represent the actual geometry very well. Other effects (e.g., the effective graded index near the surface and wave interference) are not included in the Monte Carlo model [48,63]. Some of the features beyond $\lambda >$ 10 µm observed in the experiments are similar to the model. For Type C, the diameter is

comparable to wavelength where Mie scattering plays an integral role. In general, due to irregular shapes of particles and polydispersed packing condition, the simple Monte Carlo model only achieves qualitative agreement in the mid-infrared. Nevertheless, it helps explain the absorption effect and trend of reflectance in this region. Note that the effect of polydispersion on the radiative transfer has recently been considered by a multiphase radiative transfer model in which particle groups within specified size intervals are treated as individual components [69].

IV. Discussion: Effect of Dependent Scattering

While the Monte Carlo method is a direct approach to obtain radiative properties of particle beds, it requires large computational resources that could be hard to meet especially when dealing with conjugated heat transfer problems. In addition, the physical representation of the particle bed in a Monte Carlo model is usually simplified to obtain qualitative results. The IAD calculation provides an easy access to the absorption and scattering characteristics, which is favored by available forward solutions of RTE. However, the experimental results (reflectance and transmittance) that are the inputs to IAD are not always available. Therefore, it is useful to examine whether single particle properties, which are generally available in various literatures or are relatively easy to calculate, can be used to approximate overall absorption and scattering characteristics of the packed bed. The absorption and scattering properties, including phase function, of a single particle can be obtained via the Monte Carlo method [56]. By summing up forward scattered and backscattered rays, the scattering efficiency can be calculated, and the absorption efficiency is obtained by subtracting it from unity.

The independent scattering theory assumes that light scattering from one particle is not affected by other particles and that all particles contribute equally to the overall absorption and

scattering characteristics. Therefore, the absorption and scattering coefficients of the packed bed can be calculated as follow:

$$a_{\lambda} = NC_{\text{abs},\lambda} \tag{9}$$

$$\sigma_{\lambda} = NC_{\text{sca},\lambda} \tag{10}$$

where $N=6\phi_v/(\pi d^3)$ is the number density (number of particles per volume), and $C_{{\rm abs},\lambda}$ and $C_{{\rm sca},\lambda}$ are the absorption and scattering cross sections of the particle, respectively, obtained from the Monte Carlo method. The same optical constants and specularity are used in modeling single particles.

The phase function is also determined from the Monte Carlo method using the angular information of scattered photon bundles and fitted to an HG phase function to obtain the asymmetry factor g. To compare with the IAD, the anisotropic (or true) scattering coefficient given in Eq. (10) is multiplied by (1-g) to obtain the reduced (isotropic equivalent) scattering coefficient, as listed in Table 2 (using the same symbol as σ_{λ}). The absorption coefficient from the model is obtained from Eq. (9) and listed in Table 2 at three wavelengths. The model gives results for independent scattering while the IAD takes into consideration any dependent scattering effect.

In addition to comparing the values of a_{λ} and σ_{λ} , the resulting T and R for L=1.0 mm with different sized particles are calculated and compared in Table 2 at $\lambda=0.7$ µm, 1.0 µm, and 1.7 µm. The agreement is very good for Type A albeit some differences in a_{λ} , indicating that dependent scattering effect is negligible and independent scattering model can produce reasonable results. For Type B, the model overpredicts 10-20% in a_{λ} and underpredicts 30-40% in σ_{λ} , resulting in an absolute error of about -0.07 in R and +0.04 in T. At $\lambda=1$ µm, the relative error in

T is 34%. For Type C, the model overpredicts 10-25% in a_{λ} and underpredicts 60-130% in σ_{λ} . At $\lambda=1$ µm, the model yields a scattering coefficient that is nearly half of the IAD. However, for L=1 mm, the measured T is nearly zero and R exceed 0.86, the model yield a lower reflectance with a relative error of 4-9% and a much higher transmittance. The ratio of transmittances calculated by AD using a_{λ} and σ_{λ} values from the model and from the IAD is 7.5, 3.2, and 1.7 at $\lambda=0.7$ µm, 1.0 µm, and 1.7 µm, respectively. It becomes clear that dependent scattering effects are significant for Type B particles and even stronger for Type C. The impact of dependent scattering in Type B particles mainly results from the geometric multiple scattering. For Type C, the modeled σ_{λ} is only a weak function of λ , while σ_{λ} obtained from IAD tends to increase rapidly toward shorter wavelength; this is a wave scattering effect which generally predicts a stronger scattering toward short wavelengths. As shown in Fig. 1c, Type C particles contains smaller sized fragments or voids that could give rise to such wave scattering effect.

V. Conclusions

The directional-hemispherical reflectance and transmittance of packed beds of polydispersed and irregular-shaped SiO₂ particles with different average diameters and bed thicknesses are measured and analyzed using both continuous-scale and discrete-scale modeling.

The effective absorption and scattering coefficients obtained for different sized particles from IAD in the visible and near-infrared may be applied for solution of RTE under similar conditions. The absorption by impurities of SiO₂ in the particle beds becomes significant at wavelengths from 0.4 µm to 1.8 µm, even though it is often negligible in bulk materials. The

scattering albedo is shown over 98% for all particles in the wavelength region between 1.0 μ m and 1.8 μ m.

A discrete-scale Monte Carlo method is developed to model the radiative properties by assuming monodispersed spherical particles using a specularity parameter. The model generally agrees with the measurement at wavelengths from $0.4~\mu m$ to $1.8~\mu m$, except when the transmittance is very low. The trend in the reflectance up to $15~\mu m$ is also predicted. Cavity effects increase the absorption in the phonon resonance band from $8~\mu m$ to $10~\mu m$, especially with smaller sized particles.

Using independent scattering theory, the absorption and reduced scattering coefficients are obtained and compared with IAD to demonstrate dependent scattering effect in Type B and C particles. It is shown that for Type A particles with an average diameter of 222 µm that is relatively round with small size variation, the independent scattering theory is appropriate for modeling the hemispherical radiative properties of particle beds. Since the packed bed is already dense, this conclusion should also be applicable when the bed is not densely packed.

Future studies that consider polydispersion and irregular shapes, along with a mixture of different materials, may help better understand the radiative properties of real systems.

Acknowledgements

This work was supported by the U.S. Department of Energy's Office of Energy Efficiency and Renewable Energy (EERE) under Solar Energy Technologies Office Award Number EE0008372. C.Y. was supported by the National Science Foundation (CBET-2029892). The views expressed herein do not necessarily represent the views of the U.S. Department of Energy, National Science Foundation, or the United States Government.

References

- [1] Hottel, H., Sarofim, A., Dalzell, W., and Vasalos, I., "Optical Properties of Coatings. Effect of Pigment Concentration," *AIAA Journal*, Vol. 9, No. 10, 1971, pp. 1895–1898. https://doi.org/10.2514/3.49999
- [2] Tien, C. L., "Thermal Radiation in Packed and Fluidized Beds," *Journal of Heat Transfer*, Vol. 110, No. 4b, 1988, pp. 1230–1242. https://doi.org/10.1115/1.3250623
- [3] Baillis, D., and Sacadura, J.-F., "Thermal Radiation Properties of Dispersed Media: Theoretical Prediction and Experimental Characterization," *Journal of Quantitative Spectroscopy and Radiative Transfer*, Vol. 67, No. 5, 2000, pp. 327–363. https://doi.org/10.1016/S0022-4073(99)00234-4
- [4] Wang, B. X., and Zhao, C. Y., "Modeling Radiative Properties of Air Plasma Sprayed Thermal Barrier Coatings in the Dependent Scattering Regime," *International Journal of Heat and Mass Transfer*, Vol. 89, 2015, pp. 920–928. https://doi.org/10.1016/j.ijheatmasstransfer.2015.06.017
- [5] Fu, T. R., Tang, J. Q., Chen, K., and Zhang, F., "Determination of Scattering and Absorption Coefficients of Porous Silica Aerogel Composites," *Journal of Heat Transfer*, Vol. 138, No. 3, 2016, Paper 032702. https://doi.org/10.1115/1.4031734
- [6] Ho, C. K., Christian, J. M., Romano, D., Yellowhair, J., Siegel, N., Savoldi, L., and Zanino, R., "Characterization of Particle Flow in a Free-Falling Solar Particle Receiver," *Journal of Solar Energy Engineering*, Vol. 139, No. 2, 2017, Paper 021011. https://doi.org/10.1115/1.4035258
- [7] Chen, J., Wheeler, V. M., Liu, B., Kumar, A., Coventry, J., and Lipinski, W., "Optical Characterisation of Alumina–Mullite Materials for Solar Particle Receiver Applications," *Solar Energy Materials and Solar Cells*, Vol. 230, 2021, Paper 111170. https://doi.org/10.1016/j.solmat.2021.111170
- [8] Chung, K. M., Zeng, J., Adapa, S. R., Feng, T., Bagepalli, M. V., Loutzenhiser, P. G., Albrecht, K. J., Ho, C. K., and Chen, R., "Measurement and Analysis of Thermal Conductivity of Ceramic Particle Beds for Solar Thermal Energy Storage," *Solar Energy Materials and Solar Cells*, Vol. 230, 2021, Paper 111271. https://doi.org/10.1016/j.solmat.2021.111271
- [9] Howell, J. R., Mengüç, M. P., Daun, K., and Siegel, R., *Thermal Radiation Heat Transfer*, 7th ed., CRC Press, New York, 2021.
- [10] Modest, M. F., and Mazumder, S., *Radiative Heat Transfer*, 4th ed., Academic Press, Amsterdam, 2021.
- [11] Drolen, B., and Tien, C. L., "Independent and Dependent Scattering in Packed-Sphere Systems," *Journal of Thermophysics and Heat Transfer*, Vol. 1, No. 1, 1987, pp. 63–68. https://doi.org/10.2514/3.8
- [12] Agarwal, B. M., and Mengüç, M. P., "Forward and Inverse Analysis of Single and Multiple Scattering of Collimated Radiation in an Axisymmetric System," *International*

- *Journal of Heat and Mass Transfer*, Vol. 34, No. 3, 1991, pp. 633–647. https://doi.org/10.1016/0017-9310(91)90112-R
- [13] Dombrovsky, L. A., and Baillis, D., *Thermal Radiation in Disperse Systems: An Engineering Approach*, Begell House, New York, 2010.
- [14] Brewster, M. Q., and Tien, C., "Radiative Transfer in Packed Fluidized Beds: Dependent Versus Independent Scattering," *Journal of Heat Transfer*, Vol. 104, No. 4, 1982, pp. 573–579. https://doi.org/10.1115/1.3245170
- [15] Yamada, Y., Cartigny, J., and Tien, C., "Radiative Transfer with Dependent Scattering by Particles: Part 2—Experimental Investigation," *Journal of Heat Transfer*, Vol. 108, No. 3, 1986, pp. 614–618. https://doi.org/10.1115/1.3246980
- [16] Kumar, S., and Tien, C., "Dependent Absorption and Extinction of Radiation by Small Particles," *Journal of Heat Transfer*, Vol. 112, No. 1, 1990, pp. 178–185. https://doi.org/10.1115/1.2910342
- [17] Mishchenko, M. I., 2002, "Vector Radiative Transfer Equation for Arbitrarily Shaped and Arbitrarily Oriented Particles: a Microphysical Derivation from Statistical Electromagnetics," *Applied Optics*, Vol. 41, No. 33, 2006, pp. 7114–7134. https://doi.org/10.1364/AO.41.007114
- [18] Mishchenko, M. I., Travis, L. D., and Lacis, A. A., *Multiple Scattering of Light by Particles: Radiative Transfer and Coherent Backscattering*, Cambridge University Press, Cambridge, 2006.
- [19] Pilon, L., and Viskanta, R., "Radiation Characteristics of Glass Containing Gas Bubbles," *Journal of the American Ceramic Society*, Vol. 86, No. 8, 2003, pp. 1313–1320. https://doi.org/10.1111/j.1151-2916.2003.tb03468.x
- [20] Dombrovsky, L., Randrianalisoa, J., Baillis, D., and Pilon, L., "Use of Mie Theory to Analyze Experimental Data to Identify Infrared Properties of Fused Quartz Containing Bubbles," *Applied Optics*, Vol. 44, No. 33, 2005, pp. 7021–7031. https://doi.org/10.1364/AO.44.007021
- [21] Haussener, S., Lipiński, W., Petrasch, J., Wyss, P., Steinfeld, A., "Tomographic Characterization of a Semitransparent-Particle Packed Bed and Determination of Its Thermal Radiative Properties," *Journal of Heat Transfer*, Vol. 131, 2009, Paper 072701. https://doi.org/10.1115/1.3109261
- [22] Ma, L. X., Wang, F. Q., Wang, C. A., Wang, C. C., and Tan, J. Y., "Investigation of the Spectral Reflectance and Bidirectional Reflectance Distribution Function of Sea Foam Layer by the Monte Carlo Method," *Applied Optics*, Vol. 54, No. 33, 2015, pp. 9863–9874. https://doi.org/10.1364/AO.54.009863
- [23] Zhou, J., Zhang, Y., and Chen, J. K., "Numerical Simulation of Laser Irradiation to a Randomly Packed Bimodal Powder Bed," *International Journal of Heat and Mass Transfer*, Vol. 52, Nos. 13-14, 2009, pp. 3137–3146. https://doi.org/10.1016/j.ijheatmasstransfer.2009.01.028

- [24] González-Portillo, L. F., Abbas, R., Albrecht, K., and Ho, C. K., "Analysis of Optical Properties in Particle Curtains," *Solar Energy*, Vol. 213, 2021, pp. 211–224. https://doi.org/10.1016/j.solener.2020.11.012
- [25] Chen, C., Yang, C., Ranjan, D., Loutzenhiser, P. G., and Zhang, Z. M., "Spectral Radiative Properties of Ceramic Particles for Concentrated Solar Thermal Energy Storage Applications," *International Journal of Thermophysics*, Vol. 41, 2020, Paper 152. https://doi.org/10.1007/s10765-020-02733-5
- [26] Yang, Y. S., Howell, J., and Klein, D., "Radiative Heat Transfer through a Randomly Packed Bed of Spheres by the Monte Carlo Method," *Journal of Heat Transfer*, Vol. 105, No. 2, 1983, pp. 325–332. https://doi.org/10.1115/1.3245582
- [27] Howell, J. R., "The Monte Carlo Method in Radiative Heat Transfer," *Journal of Heat Transfer*, Vol. 120, No. 3, 1998, pp. 547–560. https://doi.org/10.1115/1.2824310
- [28] Singh, B., and Kaviany, M., "Independent Theory Versus Direct Simulation of Radiation Heat Transfer in Packed Beds," *International Journal of Heat and Mass Transfer*, Vol. 34, No. 11, 1991, pp. 2869–2882. https://doi.org/10.1016/0017-9310(91)90247-C
- [29] Coquard, R., and Baillis, D., "Radiative Characteristics of Beds of Spheres Containing an Absorbing and Scattering Medium," *Journal of Thermophysics and Heat Transfer*, Vol. 19, No. 2, 2005, pp. 226–234. https://doi.org/10.2514/1.6809
- [30] Randrianalisoa, J., and Baillis, D., "Radiative Properties of Densely Packed Spheres in Semitransparent Media: A New Geometric Optics Approach," *Journal of Quantitative Spectroscopy and Radiative Transfer*, Vol. 111, No. 10, 2010, pp. 1372–1388. https://doi.org/10.1016/j.jqsrt.2010.01.014
- [31] Randrianalisoa, J., and Baillis, D., "Radiative Transfer in Dispersed Media: Comparison between Homogeneous Phase and Multiphase Approaches," *Journal of Heat Transfer*, Vol. 132, 2010, Paper 023405. https://doi.org/10.1115/1.4000237
- [32] Petrasch, J., Haussener, S., and Lipiński, W., "Discrete vs. Continuous-Scale Simulation of Radiative Transfer in Semitransparent Two-Phase Media," *Journal of Quantitative Spectroscopy and Radiative Transfer*, Vol. 112, 2011, pp. 1450–1459. https://doi.org/10.1016/j.jqsrt.2011.01.025
- [33] Wang, C. A., Ma, L. X., Tan, J. Y., and Liu, L. H., "Study of Radiative Transfer in 1D Densely Packed Bed Layer Containing Absorbing–Scattering Spherical Particles," *International Journal of Heat and Mass Transfer*, Vol. 102, 2016, pp. 669–678. https://doi.org/10.1016/j.ijheatmasstransfer.2016.06.065
- [34] Coquard, R., and Baillis, D., "Radiative Characteristics of Opaque Spherical Particles Beds: A New Method of Prediction," *Journal of Thermophysics and Heat Transfer*, Vol. 18, No. 2, 2004, pp. 178–186. https://doi.org/10.2514/1.5082
- [35] Coquard, R., and Baillis, D., "Radiative Characteristics of Beds Made of Large Spheres Containing an Absorbing and Scattering Medium," *International Journal of Thermal Sciences*, Vol. 44, 2005, pp. 926–932. https://doi.org/10.1016/j.ijthermalsci.2005.03.009

- [36] Kamiuto, K., "Correlated Radiative Transfer in Packed-Sphere Systems," *Journal of Quantitative Spectroscopy and Radiative Transfer*, Vol. 43, No. 1, 1990, pp. 39–43. https://doi.org/10.1016/0022-4073(90)90063-C
- [37] Kamiuto, K., Iwamoto, M., Nishimura, T., and Sato, M., "Albedos and Asymmetry Factors of the Phase Functions for Packed-Sphere Systems," *Journal of Quantitative Spectroscopy and Radiative Transfer*, Vol. 46, No. 4, 1991, pp. 309–316. https://doi.org/10.1016/0022-4073(91)90095-8
- [38] Singh, B., and Kaviany, M., "Modelling Radiative Heat Transfer in Packed Beds," *International Journal of Heat and Mass Transfer*, Vol. 35, No. 6, 1992, pp. 1397–1405. https://doi.org/10.1016/0017-9310(92)90031-M
- [39] Brewster, M. Q., "Volume Scattering of Radiation in Packed Beds of Large, Opaque Spheres," *Journal of Heat Transfer*, Vol. 126, 2004, pp. 1048–1050. https://doi.org/10.1115/1.1795247
- [40] Tancrez, M., and Taine, J., "Direct Identification of Absorption and Scattering Coefficients and Phase Function of a Porous Medium by a Monte Carlo Technique," *International Journal of Heat and Mass Transfer*, Vol. 47, No. 2, 2004, pp. 373-383. https://doi.org/10.1016/S0017-9310(03)00146-7
- [41] Zeghondy, B., Iacona, E., and Taine, J., "Determination of the Anisotropic Radiative Properties of a Porous Material by Radiative Distribution Function Identification (RDFI)," *International Journal of Heat and Mass Transfer*, Vol. 49, 2006, pp. 2810–2819. https://doi.org/10.1016/j.ijheatmasstransfer.2006.02.034
- [42] Zarrouati, M., Enguehard, F., and Taine, J., "Radiative Transfer within Strongly Non Homogeneous Porous Media: Application to a Slab of Packed Particles," *International Journal of Heat and Mass Transfer*, Vol. 91, 2015, pp. 936–947. https://doi.org/10.1016/j.ijheatmasstransfer.2015.08.024
- [43] Lipiński, W., Petrasch, J., and Haussener, S., "Application of the Spatial Averaging Theorem to Radiative Heat Transfer in Two-Phase Media," *Journal of Quantitative Spectroscopy and Radiative Transfer*, Vol. 111, No. 1, 2010, pp. 253–258. https://doi.org/10.1016/j.jqsrt.2009.08.001
- [44] Kamiuto, K., Iwamoto, M., Sato, M., and Nishimura, T., "Radiation-Extinction Coefficients of Packed-Sphere Systems," *Journal of Quantitative Spectroscopy and Radiative Transfer*, Vol. 45, No. 2, 1991, pp. 93–96. https://doi.org/10.1016/0022-4073(91)90103-W
- [45] Hendricks, T. J., and Howell, J. R., "Absorption, Scattering Coefficients and Scattering Phase Function in Reticulated Porous Ceramics," *Journal of Heat Transfer*, Vol. 118, 1996, pp. 79–87. https://doi.org/10.1115/1.2824071
- [46] Sacadura, J.-F., and Baillis, D., "Experimental Characterization of Thermal Radiation Properties of Dispersed Media," *International Journal of Thermal Sciences*, Vol. 41, 2002, pp. 699–707. https://doi.org/10.1016/S1290-0729(02)01365-0

- [47] Ganesan, K., and Lipiński, W., "Experimental Determination of Spectral Transmittance of Porous Cerium Dioxide in the Range 900–1700 nm," *Journal of Heat Transfer*, Vol. 133, No. 10, 2011, Paper 104501. https://doi.org/10.1115/1.4003970
- [48] Yang, P., Cheng, Q., and Zhang, Z. M., "Radiative Properties of Ceramic Al₂O₃, AlN and Si₃N₄—II: Modeling," *International Journal of Thermophysics*, Vol. 38, 2017, Paper 124. https://doi.org/10.1007/s10765-017-2259-x
- [49] D. Baillis, D., Raynaud, M., and Sacadura, J.-F., "Spectral Radiative Properties of Open-Cell Foam Insulation," *Journal of Thermophysics and Heat Transfer*, Vol. 13, No. 3, 1999, pp. 292–298. https://doi.org/10.2514/2.6457
- [50] Zhao, C. Y., Lu, T. J., and Hodson, H. P., "Thermal Radiation in Ultralight Metal Foams with Open Cells," *International Journal of Heat and Mass Transfer*, Vol. 47, Nos. 14–16, 2004, pp. 2927–2939. https://doi.org/10.1016/j.ijheatmasstransfer.2004.03.006
- [51] Li, Q., Lee, B. J., Zhang, Z. M., and Allen, D. W., "Light Scattering of Semitransparent Sintered Polytetrafluoroethylene Films," *Journal of Biomedical Optics*, Vol. 13, No. 5, 2008, Paper 054064. https://doi.org/10.1117/1.2992485
- [52] Yang, P., Chen, C., and Zhang, Z. M., "A Dual-Layer Structure with Record-High Solar Reflectance for Daytime Radiative Cooling," *Solar Energy*, Vol. 169, 2018, pp. 316–324. https://doi.org/10.1016/j.solener.2018.04.031
- [53] Prahl, S. A., van Gemert, M. J. C., and Welch, A. J., "Determining the Optical Properties of Turbid Media by Using the Adding–Doubling Method," *Applied Optics*, Vol. 32, No. 4, 1993, pp. 559–568 (1993). https://doi.org/10.1364/AO.32.000559
- [54] Bashkatov, A. N., Genina1, E. A., Kochubey, V. I., and Tuchin, V. V., "Optical Properties of Human Skin, Subcutaneous and Mucous Tissues in the Wavelength Range from 400 to 2000 nm," *Journal of Physics D: Applied Physics*, Vol. 38, No. 15, 2005, pp. 2543–2555. http://doi:10.1088/0022-3727/38/15/004
- [55] Yang, P., and Zhang, Z. M., "Bidirectional Reflection of Semitransparent Polytetrafluoroethylene (PTFE) Sheets on a Silver Film," *International Journal of Heat and Mass Transfer*, Vol. 148, 2020, Paper 118992. https://doi.org/10.1016/j.ijheatmasstransfer.2019.118992
- [56] Jeong, S. Y., Chen, C., Ranjan, D., Loutzenhiser, P. G., and Zhang, Z. M., "Measurements of Scattering and Absorption Properties of Submillimeter Bauxite and Silica Particles," *Journal of Quantitative Spectroscopy and Radiative Transfer*, Vol. 276, 2021, Paper 107923. https://doi.org/10.1016/j.jqsrt.2021.107923
- [57] Hespel, L., Mainguy, S., and Greffet, J.-J., "Radiative Properties of Scattering and Absorbing Dense Media: Theory and Experimental Study," *Journal of Quantitative Spectroscopy and Radiative Transfer*, Vol. 77, 2003, pp. 193–210. https://doi.org/10.1016/S0022-4073(02)00123-1
- [58] Lipiński, W., Guillot, E., Olalde, G., and Steinfeld, A., "Transmittance Enhancement of Packed-Bed Particulate Media," *Experimental Heat Transfer*, Vol. 21, No. 1, 2008, pp. 73–82. https://doi.org/10.1080/08916150701647843

- [59] Jäger, K., Lipiński, W., Katzgraber, H. G., and Steinfeld, A., "Determination of Thermal Radiative Properties of Packed-Bed Media Containing a Mixture of Polydispersed Particles," *International Journal of Thermal Sciences*, Vol. 48, No. 8, 2009, pp. 1510–1516. https://doi.org/10.1016/j.ijthermalsci.2008.12.006
- [60] Coray, P., Lipiński, W., and Steinfeld, A., "Experimental and Numerical Determination of Thermal Radiative Properties of ZnO Particulate Media," *Journal of Heat Transfer*, Vol. 132, 2010, Paper 012701. https://doi.org/10.1115/1.3194763
- [61] Marti, J., Roesle, M., and Steinfeld, A., "Experimental Determination of the Radiative Properties of Particle Suspensions for High-Temperature Solar Receiver Applications," *Heat Transfer Engineering*, Vol. 35, No. 3, 2014, pp. 272–280. https://doi.org/10.1080/01457632.2013.825173
- [62] Webpages: https://omlc.org/software/iad/index.html (last accessed January 17, 2022).
- [63] Zhang, Z. M., *Nano/Microscale Heat Transfer*, 2nd ed., Springer, Cham, Switzerland, 2020.
- [64] Philipp, H. R., "Silicon Dioxide (SiO₂), Type α (Crystalline)," in *Handbook of Optical Constants of Solids*, edited by E. D. Palik, Academic Press, New York, 1998, pp. 719–747.
- [65] Kitamura, R., Pilon, L., and Jonasz, M., "Optical Constants of Silica Glass from Extreme Ultraviolet to Far Infrared at near Room Temperature," *Applied Optics*, Vol. 46, No. 33, 2007, pp. 8118–8133. https://doi.org/10.1364/AO.46.008118
- [66] Tan, C. Z., "Optical Interference in Overtones and Combination Bands in α-Quartz," Journal of Physics and Chemistry of Solids, Vol. 64, No. 1, 2003, pp. 121–125. https://doi.org/10.1016/S0022-3697(02)00271-8
- [67] Wood, D. L., "Infrared Absorption of Defects in Quartz," *Journal of Physics and Chemistry of Solids*, Vol. 13, Nos. 3–4, 1960, pp. 326–336. https://doi.org/10.1016/0022-3697(60)90017-2
- [68] Atiganyanun, S., Plumley, J. B., Han, S. J., Hsu, K. Cytrynbaum, J., Peng, T. L., Han, S. M., and Han S. E., "Effective Radiative Cooling by Paint-Format Microsphere-Based Photonic Random Media," ACS Photonics, Vol. 5, 2018, pp. 1181–1187. https://doi.org/10.1021/acsphotonics.7b01492
- [69] Chen, J., Kumar, A., Coventry, J., Kim, J.-S., and Lipinski, W., "Numerical Modelling of Radiative Heat Transfer in a Polydispersion of Ceramic Particles under Direct High-Flux Solar Irradiation," *Journal of Quantitative Spectroscopy and Radiative Transfer*, Vol. 278, 2022, Paper 108008. https://doi.org/10.1016/j.jqsrt.2021.108008

Table 1. Particle information and polynomial fitting parameters

Sample identification	Type A	Type B	Type C
Average diameter, d (μ m)	222	150	40
Particle volume fraction, ϕ_v	0.68	0.60	0.72

Polynomial fitting of absorption and scattering coefficients a_{λ} (or σ_{λ}) = $b_0 + b_1 \lambda + b_2 \lambda^2 + ...$ (λ in μ m)

$$a_{\lambda}$$
 (or σ_{λ}) = $b_0 + b_1 \lambda + b_2 \lambda^2 + ...$ (λ in μ m)

Fitted parameter (all in mm ⁻¹)	Type A a_{λ}	σ_{λ}	Type B a_{λ}	σ_{λ}	Type C a_{λ}	σ_{λ}
Degree of polynomial	4	4	6	4	6	2
b_0	0.90700	3.395	12.726	10.739	8.5780	80.624
b_1	-2.4610	-2.440	-64.934	-9.8200	-43.566	-43.224
b_2	2.6400	2.736	137.47	11.507	93.325	11.449
b_3	-1.2650	-1.399	-152.68	-6.2870	-105.98	_
b_4	0.22600	0.2700	93.631	1.2910	66.818	_
b_5		_	-30.057		-22.107	
b_6	_		3.9480		2.9950	

Table 2. Absorption coefficient and reduced scattering coefficient obtained from independent scattering model and from experiments using IAD, along with the calculated transmittance and reflectance using AD for a 1.0 mm thickness particle bed

	λ (μm)	a_{λ} (mm ⁻¹)	$\sigma_{\lambda} \ (ext{mm}^{-1})$	R	T
Type A					
Model	0.7	1.15E-01	2.61	0.485	0.329
IAD	0.7	9.78E-02	2.61	0.498	0.341
Model	1.0	4.77E-02	2.64	0.538	0.377
IAD	1.0	4.65E-02	2.56	0.532	0.385
Model	1.7	2.01E-02	2.63	0.561	0.401
IAD	1.7	2.55E-02	2.54	0.547	0.406
Туре В					
Model	0.7	1.76E-01	5.31	0.587	0.145
IAD	0.7	1.57E-01	7.66	0.660	0.099
Model	1.0	1.24E-01	5.35	0.625	0.168
IAD	1.0	1.04E-01	7.43	0.695	0.125
Model	1.7	7.16E-02	5.40	0.671	0.197
IAD	1.7	5.87E-02	7.19	0.732	0.156
Type C					
Model	0.7	1.53E-01	24.48	0.798	0.015
IAD	0.7	1.39E-01	55.98	0.867	0.002
Model	1.0	6.65E-02	24.54	0.858	0.032
IAD	1.0	6.25E-02	48.85	0.902	0.010
Model	1.7	2.64E-02	24.52	0.898	0.049
IAD	1.7	1.97E-02	40.23	0.932	0.029

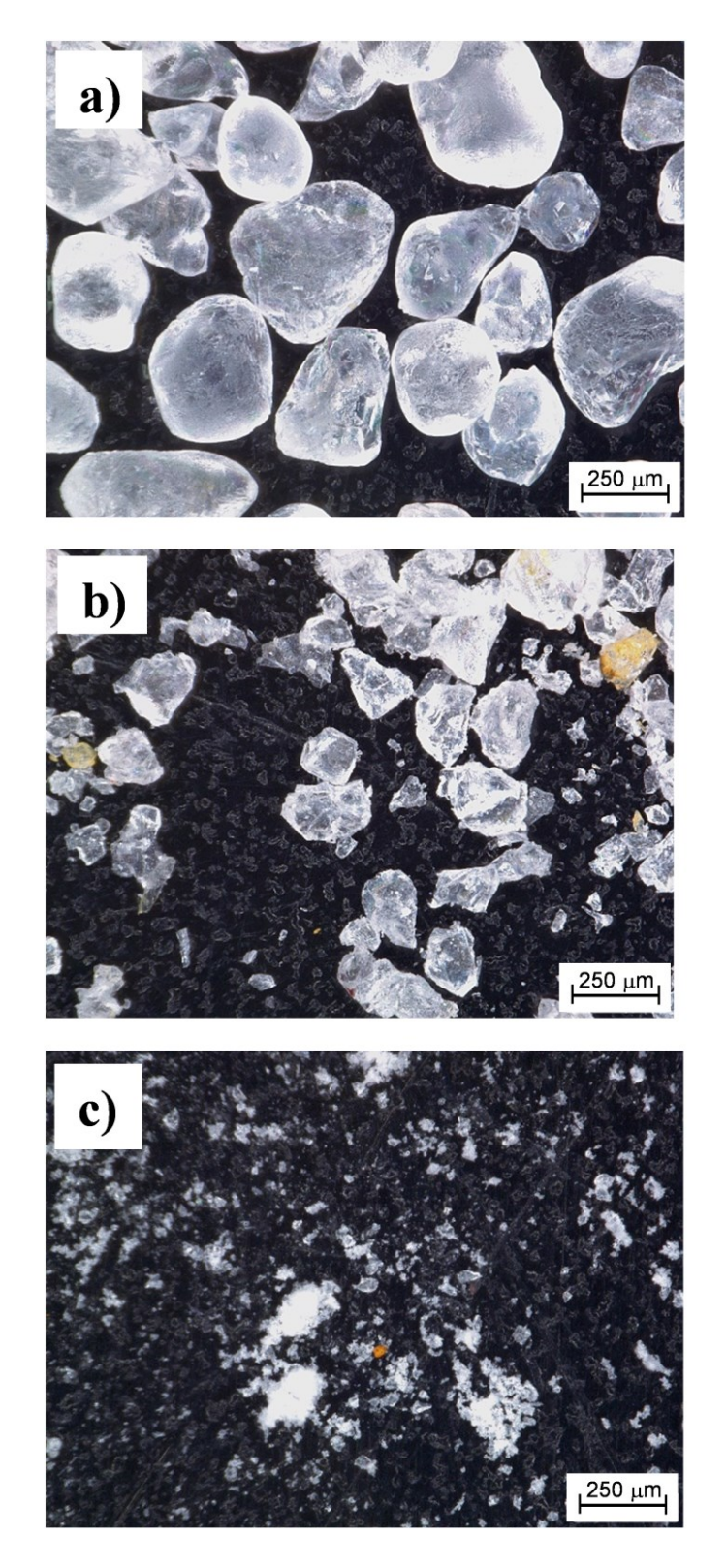


Fig. 1. Digital microscope images of the three types of SiO₂ particles: a) Type A with $d=222~\mu m$; b) Type B with $d=150~\mu m$; c) Type C with $d=40~\mu m$.

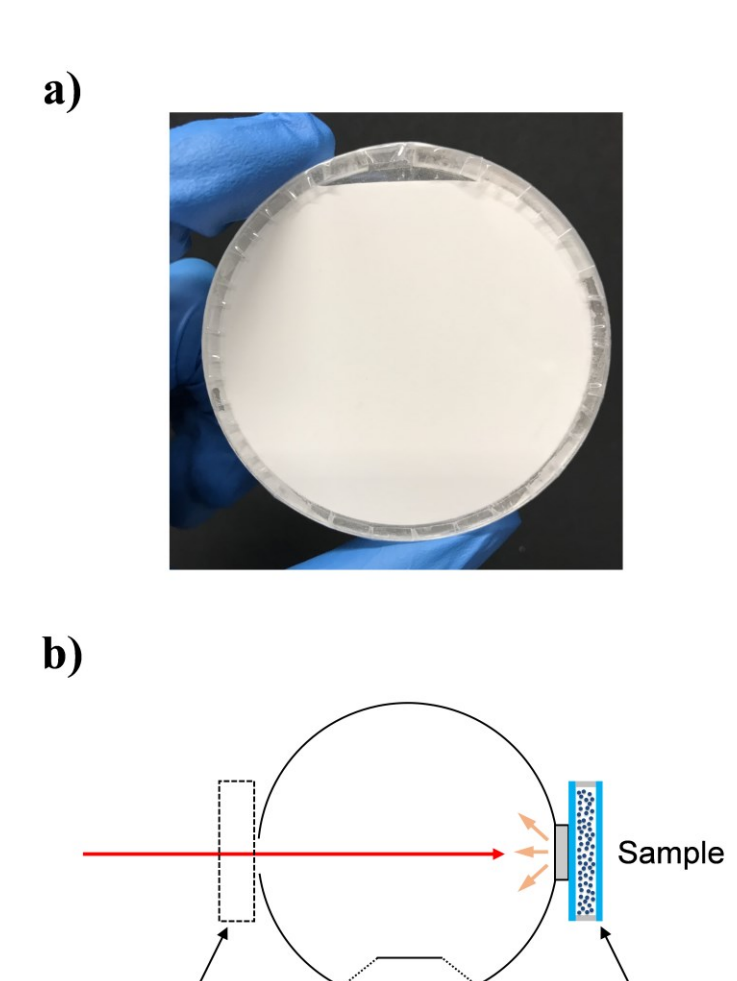


Fig. 2. Measurement of windowed particle bed: a) a picture of particles in a windowed sample holder; b) schematic illustration of the integrating sphere measurement of directional—hemispherical transmittance and reflectance of the sample.

Detector

Reflectance measurement

Transmittance

measurement

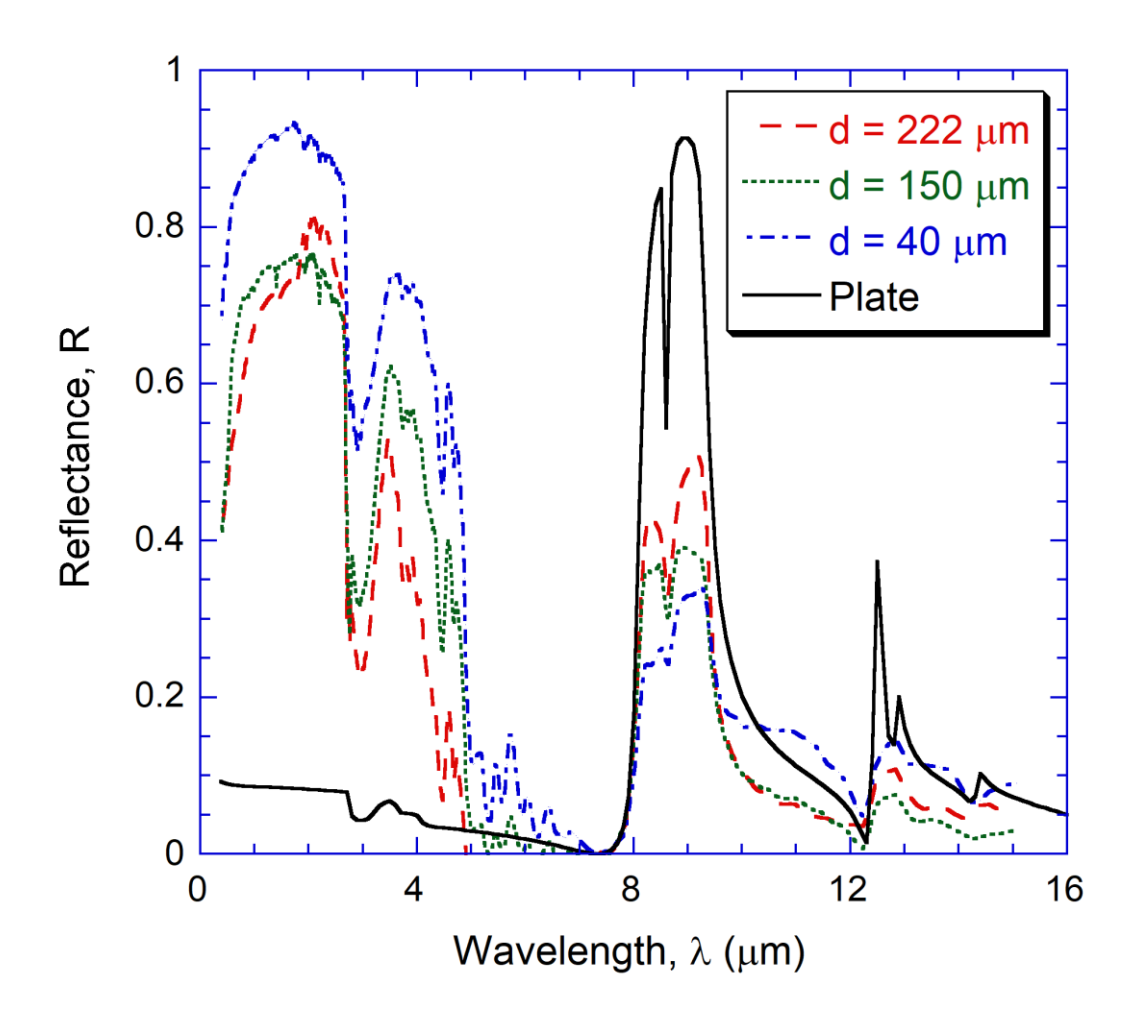


Fig. 3. Measured reflectance spectra of SiO_2 particle beds at L=6.2 mm, and the calculated reflectance spectrum for a flat plate having the same thickness.

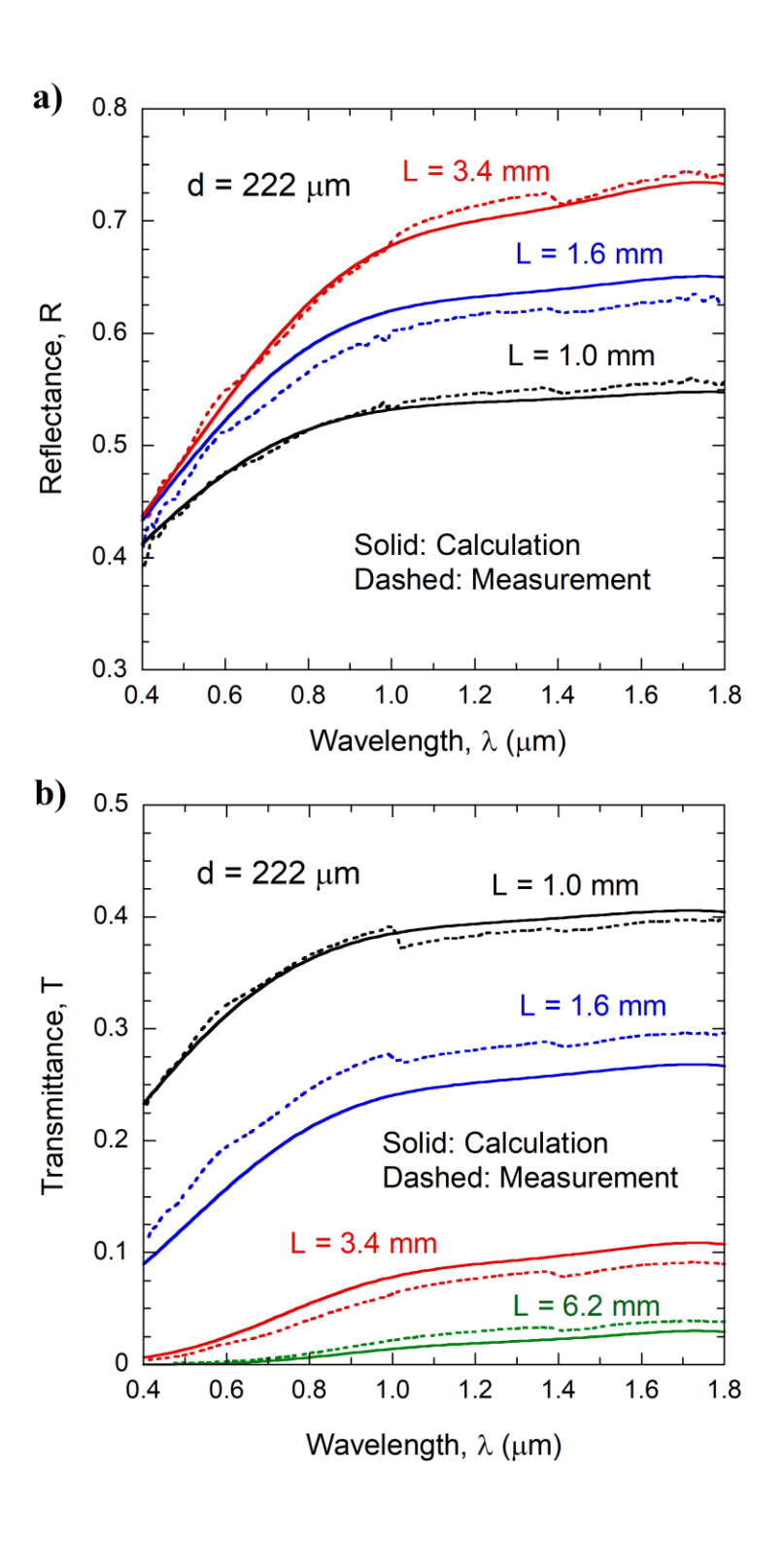


Fig. 4. Measured and modeled radiative properties of packed beds for Type A particles ($d = 222 \mu m$) with different thicknesses: a) reflectance; b) transmittance.

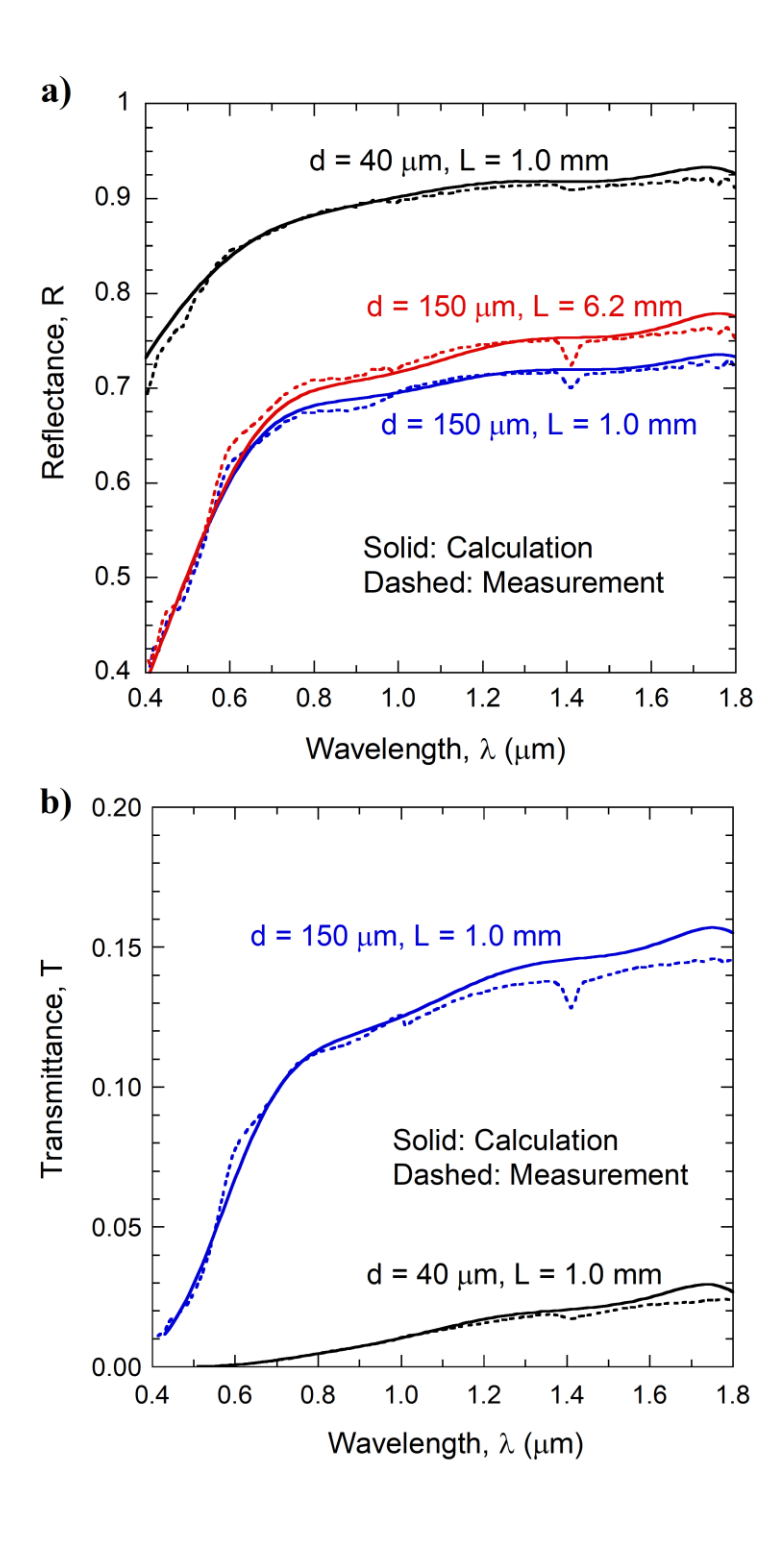


Fig. 5. Measured and modeled radiative properties of packed beds for Type B and C particles ($d = 150 \mu m$ and $40 \mu m$): a) reflectance; b) transmittance.

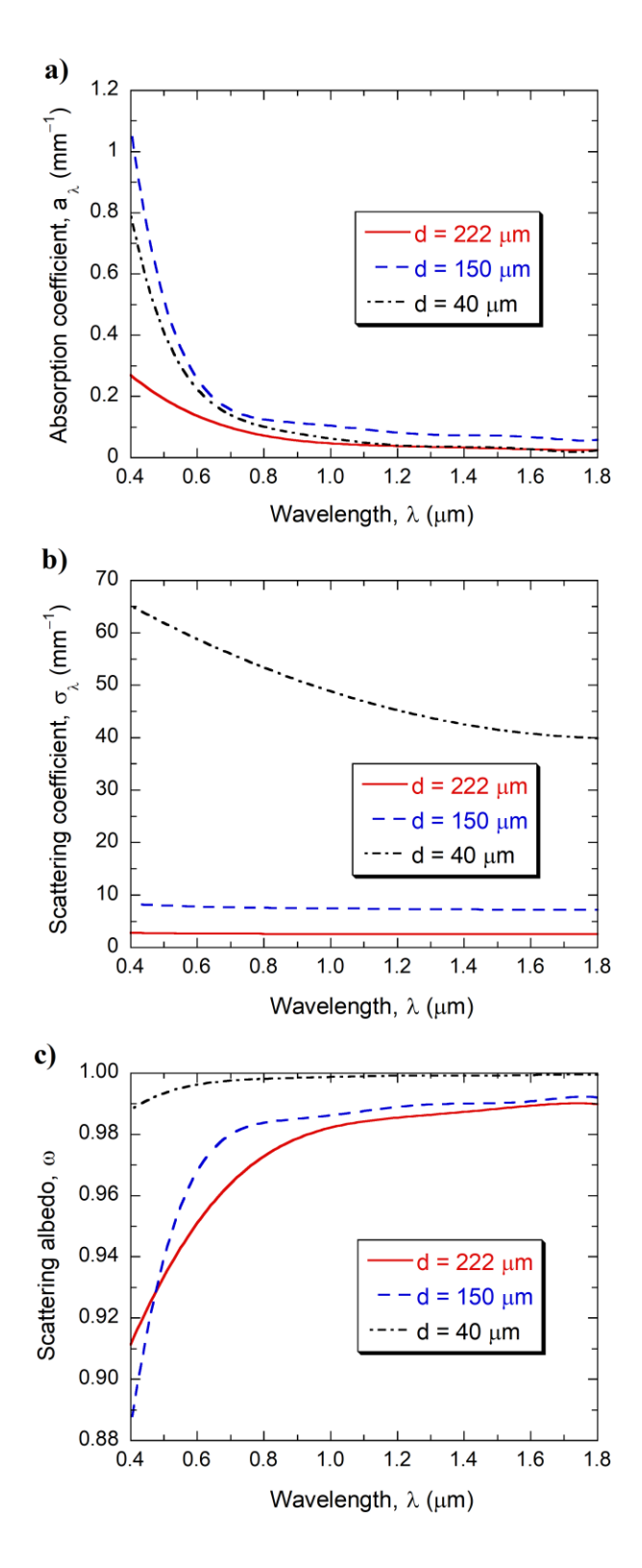


Fig. 6. Parameters retrieved from the IAD method for the three types of particles: a) absorption coefficient; b) scattering coefficient; c) scattering albedo.

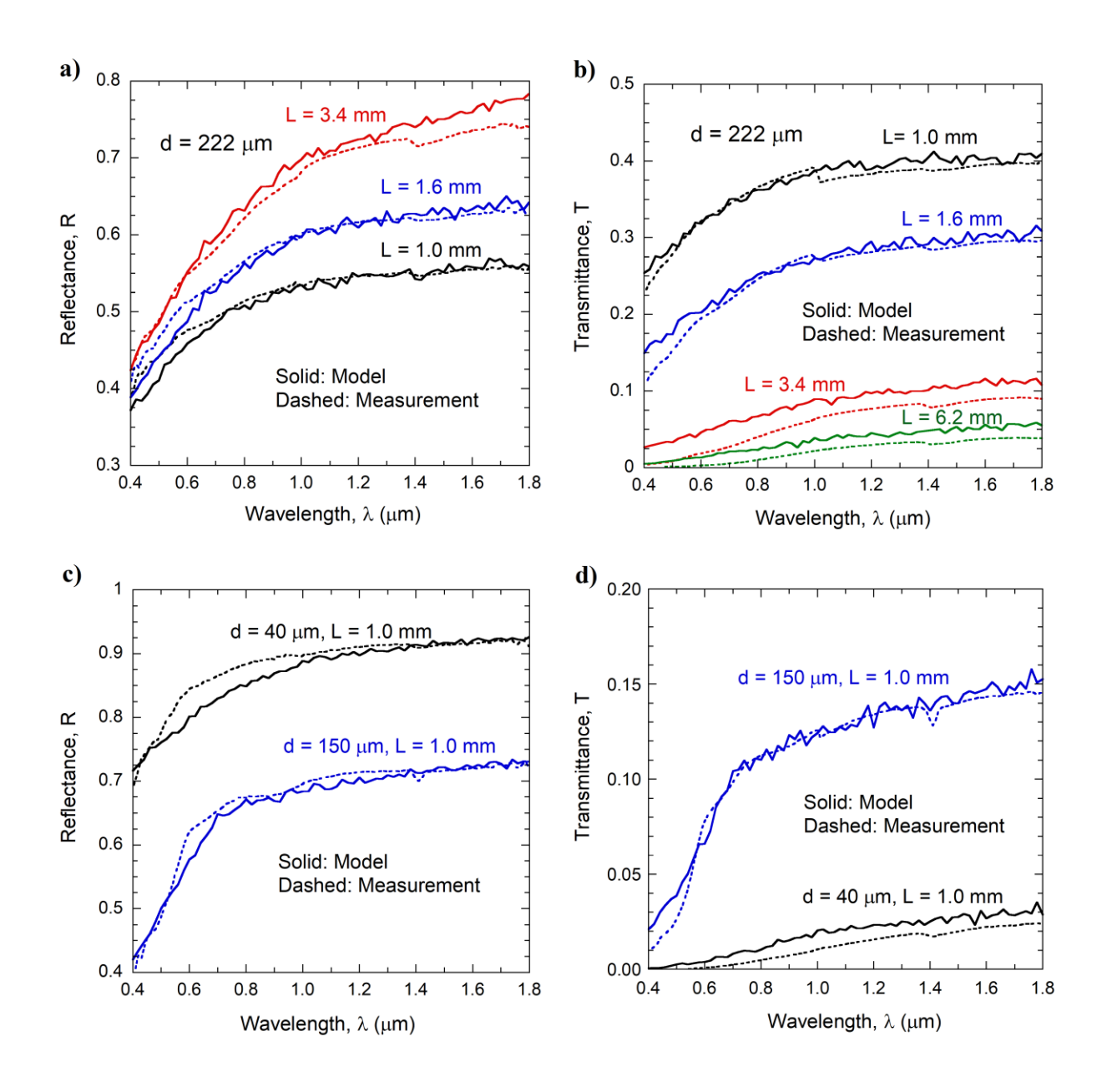


Fig. 7. Measured and modeled radiative properties of the particle beds using the Monte Carlo method for L = 1.0 mm: a) reflectance for Type A; b) transmittance for Type A; c) reflectance for Type B and C; d) transmittance for Type B and C.

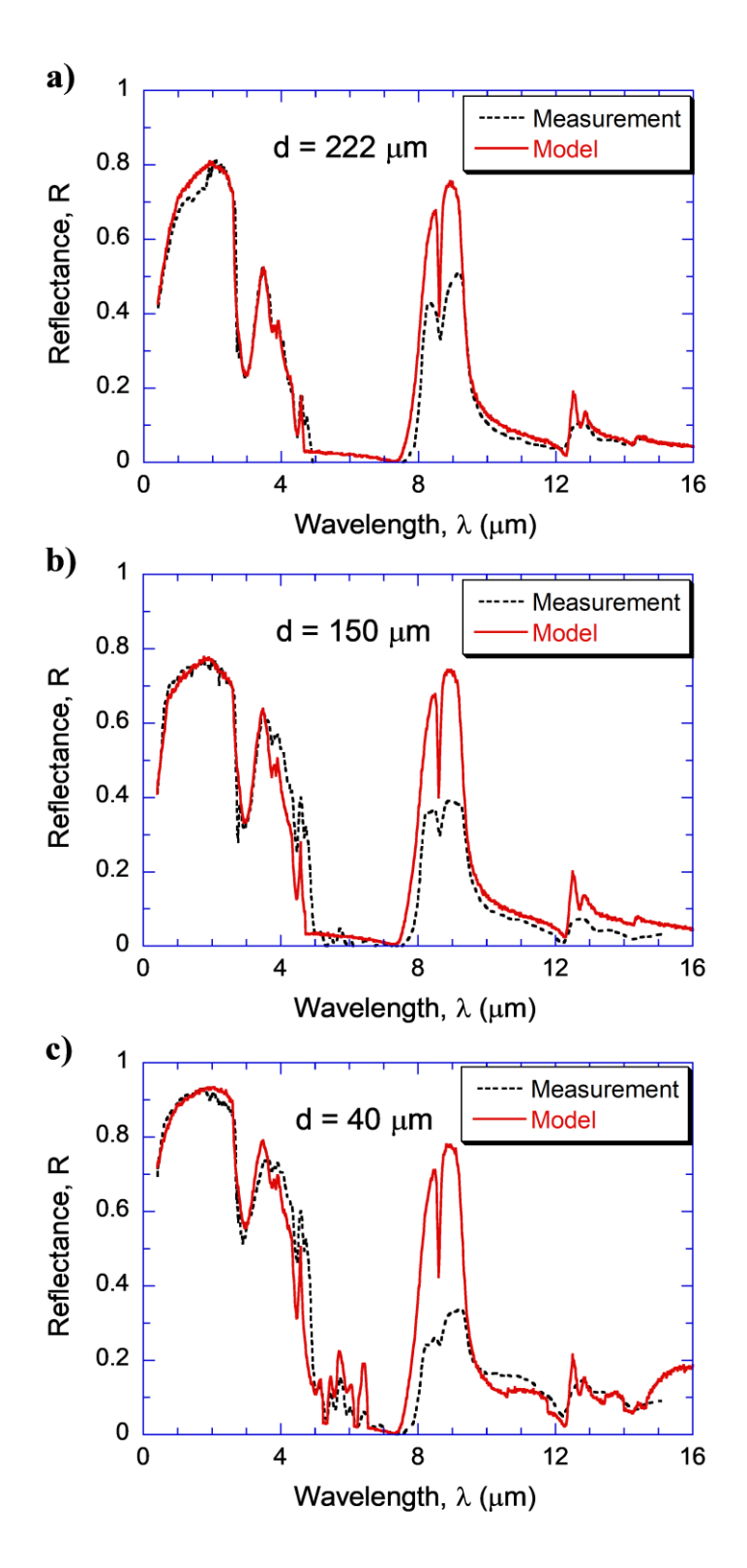


Fig. 8. Measured and modeled reflectance of SiO_2 particle beds using the Monte Carlo method for L = 6.2 mm: a) Type A; b) Type B; c) Type C.